Coherent interface structures and intergrain Josephson coupling in dense MgO/Mg2Si/MgB2 nanocomposites

Ueno, Katsuya ; Nagashima, Yukihito ; Seto, Yusuke ; Matsumoto, Megumi ; Sakurai, Takahiro ; Ohta, Hitoshi ; Takahashi, Kazuyuki ; Uchino,…

(Citation)
Journal of Applied Physics,120(1):015102-015102

(Issue Date)
2016-07-07

(Resource Type)
journal article

(Version)
Version of Record

Coherent interface structures and intergrain Josephson coupling in dense $MgO/Mg_2Si/MgB_2$ nanocomposites

Katsuya Ueno, Yukihito Nagashima, Yusuke Seto, Megumi Matsumoto, Takahiro Sakurai, Hitoshi Ohta, Kazuyuki Takahashi, and Takashi Uchino'

Citation: Journal of Applied Physics **120**, 015102 (2016); doi: 10.1063/1.4954875
View online: http://dx.doi.org/10.1063/1.4954875
View Table of Contents: http://aip.scitation.org/toc/jap/120/1
Published by the American Institute of Physics

Coherent interface structures and intergrain Josephson coupling in dense $MgO/Mg_2Si/MgB_2$ nanocomposites

Katsuya Ueno,[1] Yukihito Nagashima,[2] Yusuke Seto,[3] Megumi Matsumoto,[4] Takahiro Sakurai,[4] Hitoshi Ohta,[5] Kazuyuki Takahashi,[1] and Takashi Uchino[1,a)]
[1]*Department of Chemistry, Graduate School of Science, Kobe University, Nada, Kobe 657-8501, Japan*
[2]*Nippon Sheet Glass Co., Ltd., Konoike, Itami 664-8520, Japan*
[3]*Department of Planetology, Graduate School of Science, Kobe University, Nada, Kobe 657-8501, Japan*
[4]*Center for Support to Research and Education Activities, Kobe University, Nada, Kobe 657-8501, Japan*
[5]*Molecular Photoscience Research Center, Kobe University, Nada, Kobe 657-8501, Japan*

(Received 13 February 2016; accepted 14 June 2016; published online 1 July 2016)

Many efforts are under way to control the structure of heterointerfaces in nanostructured composite materials for designing functionality and engineering application. However, the fabrication of high-quality heterointerfaces is challenging because the crystal/crystal interface is usually the most defective part of the nanocomposite materials. In this work, we show that fully dense insulator (MgO)/semiconductor(Mg_2Si)/superconductor(MgB_2) nanocomposites with atomically smooth and continuous interfaces, including epitaxial-like MgO/Mg_2Si interfaces, are obtained by solid phase reaction between metallic magnesium and a borosilicate glass. The resulting nanocomposites exhibit a semiconductor-superconducting transition at 36 K owing to the MgB_2 nanograins surrounded by the MgO/Mg_2Si matrix. This transition is followed by the intergrain phase-lock transition at ~24 K due to the construction of Josephson-coupled network, eventually leading to a near-zero resistance state at 17 K. The method not only provides a simple process to fabricate dense nanocomposites with high-quality interfaces, but also enables to investigate the electric and magnetic properties of embedded superconducting nanograins with good intergrain coupling. *Published by AIP Publishing.* [http://dx.doi.org/10.1063/1.4954875]

I. INTRODUCTION

The field of nanocomposites stimulates the study of multiphase material consisting of nanoscale (≲100 nm) materials with different mechanical, electric, magnetic, and optical properties.[1–3] The potential of nanocomposites lies in their multifunctionality, i.e., the possibility of realizing unique interactions of properties that are unachievable with traditional bulk materials.[4–6] However, the efforts to realize the potential are challenging due to a number of factors, including the distribution in size and dispersion of the nanoscale constituents and the crystallographic quality of their interfacial structures need to be considered.[7] As for ceramic-based nanocomposites, various sintering techniques, such as spark plasma sintering (SPS)[1] and hot isostatic pressing (HIP)[8] have been employed to obtain dense nanocomposite materials with improved interface quality. Although the above sintering techniques are promising, the atomistic mechanisms responsible for the grain boundary diffusion phenomena are often too complex to be controlled, sometimes leading to unwanted grain growth.[9,10] In that sense, an approach alternative to conventional sintering techniques is desirable for further development and improvement of nanocrystalline ceramics.[11] In this work, we propose a method to synthesize fully dense nanocomposites using solid phase reaction between metallic magnesium and bulk borosilicate glass. Since borosilicate glass includes SiO_2 and B_2O_3 as glass forming oxides, the reactions are expected to proceed as follows:[12,13]

$$4Mg + SiO_2 \rightarrow 2MgO + Mg_2Si, \quad (1)$$

$$4Mg + B_2O_3 \rightarrow 3MgO + MgB_2. \quad (2)$$

We find that nearly 100% dense nanocomposite consisting of MgO (insulator), Mg_2Si (semiconductor), and MgB_2 (superconductor) is obtained without performing post-sintering heat treatments. Also, the reactions lead to a self-grown periodic layered structure consisting of alternating MgO- and $MgSi_2$-rich layers. We further reveal that atomically coherent interfaces are formed at the boundary of the MgO- and $MgSi_2$-rich layers. The resulting composite shows a rather low resistivity of a few Ωcm at room temperature although it comprises more than 40 vol. % of MgO. Moreover, the nanocomposite shows a semiconductor-superconducting transition at 36 K irrespective of a small volume fraction of MgB_2 in the composite. Resistive and magnetic measurements demonstrate that the superconducting transition proceeds in two stages, namely, the intragrain transition at 36 K due to the embedded MgB_2 nanograins and the intergrain transition at ~24 K induced by the Josephson coupled network over the $MgO/Mg_2Si/MgB_2$ nanostructures. Thus, the present approach can pave the way towards the creation of high-quality $MgO/Mg_2Si/MgB_2$ interfaces, and the related strong Josephson junctions consisting of physically remote but electrically connected MgB_2 nanograins.

a)Electronic mail: uchino@kobe-u.ac.jp

II. EXPERIMENTAL PROCEDURES

The dense $MgO/Mg_2Si/MgB_2$ nanocomposite was prepared by reacting metallic Mg with sodium borosilicate glass with a typical composition of $68SiO_2$-$24B_2O_3$-$8Na_2O$ (mol. %) at 700 °C for 5 h under Ar environment. The composition of the glass was selected because of the following reasons. When the amount of B_2O_3 becomes higher than 30–40 mol. %, the glass becomes softer and more fluid during reaction with Mg. This prevents the formation of well-ordered interfaces in the product. On the other hand, a clear superconducting transition was not observed when we used the glass with B_2O_3 concentration below ~20 mol. %. In this work, Na_2O was added to facilitate stable glass formation because metastable two-liquid immiscibility generally occurs in the binary SiO_2-B_2O_3 system.[14] As will be shown below, Na_2O is likely to be expelled from the reaction zone during reaction between Mg and the glass, and the resulting composite consists practically of MgO, Mg_2Si, and MgB_2.

A sodium borosilicate glass with the composition of $68SiO_2$-$24B_2O_3$-$8Na_2O$ (in mol. %) was prepared using a conventional melt-quenching method. Commercial powders of SiO_2, B_2O_3, and Na_2CO_3 were mixed and melted in a platinum-rhodium crucible at 1400–1500 °C for 2 h. The melt was then poured onto a steel plate and was annealed at 600 °C for 24 h. The resulting glass was cut into cubic pieces with a size of $10 \times 10 \times 10$ mm and polished with cerium oxide. Then, the cubic glass sample and ~1 g of Mg powders were put in a cylindrical alumna crucible with an internal diameter of 36 mm and a height of 27 mm. This crucible was located inside a larger rectangular ($90 \times 90 \times 50$ mm) alumina crucible, which was closed with a 4-mm thick alumina lid. This set of crucibles was placed in a box-type electric furnace. The furnace was evacuated to a pressure down to ~30 Pa and purged with argon. In order to promote the reaction between Mg and sodium borosilicate glass, the temperature of the furnace was raised to 700 °C at a rate of ~10 °C/min and kept for 5 h under flowing argon environment. After the heating process, the reaction layer with a thickness of ~0.5 mm was developed at all the six surfaces of the cubic glass sample. We then removed the reaction layers from the unreacted region of the glass. As a result, we obtained granules of samples with sizes of approximately 1 to 2 mm. For structural and property characterization, we used these granular samples.

The density of the sample was measured by a helium pycnometer (Shimadzu, AccuPyc II 1330). Powder X-ray diffraction (XRD) patterns were obtained with an X-ray diffractometer (Rigaku, SmartLab) using Cu Kα radiation (wavelength $\lambda = 1.5418$ Å). For the XRD measurements, the sample granules were further crushed into fine powder. Scanning electron microscopy (SEM) and energy dispersive X-ray (EDX) spectroscopy were conducted with a scanning electron microscope (JEOL, JSM-5610VS) with an EDX spectrometer. X-ray photoelectron spectroscopy (XPS) was carried out with a XPS spectrometer (Ulvac-Phi, PHI X-tool) utilizing Al Kα X-rays (1486.6 eV). High-resolution transmission electron microscopy (HR-TEM) measurements were performed with a (scanning) transmission electron microscope (JEOL, JEM-2100F) equipped with an EDX spectrometer and a high angle annular dark field detector (HAADF) operated at an acceleration voltage of 200 kV. An ion slicer was used to obtain a thin section for transmission electron microscopy (TEM) measurements. A commercial superconducting quantum interference device (SQUID) magnetometer (Quantum Design, MPMS-XL) equipped with the reciprocating sample option (RSO) was used for magnetization measurements. For the SQUID measurements, several pieces of granular samples (1–2 mm in size) were weighted (51.20 mg) and mounted on a plastic sample holder. Thus, the effect of sample orientation with respect to the applied filed on magnetization is averaged out and hence cannot be evaluated. Magnetization (M) in a zero-field-cooled (ZFC) states was measured by cooling the sample initially in a zero field to 2 K, and ZFC magnetization was recorded in an applied magnetic field (H) as the temperature is increased. When the temperature reached 300 K, the sample was gradually cooled under the applied filed to obtain the field-cooled (FC) magnetization. The $M(H)$ curves ware measured at several different temperatures after zero-field cooling. All the $M(H)$ curves given in this work are shown after correcting for the diamagnetic component of the sample at 40 K. A four-terminal contact configuration was used for temperature-dependent resistivity measurements of the periodic layered structure. Four-terminal contacts were fabricated on the cross section of the product along the direction parallel to the layered structure. During the resistivity measurements, the temperature was varied from 4.2 to 300 K using liquid helium.

III. RESULTS

A. Structural characterization

Figure 1 shows a typical X-ray diffraction (XRD) pattern of the reaction zone. The XRD pattern exhibits the diffraction peaks corresponding to MgO, Mg_2Si, and MgB_2, confirming that the reaction proceeds according to Eqs. (1) and (2). The Scherrer formula yields a lower limit of the grain sizes of 30, 45, and 15 nm for MgO, Mg_2Si, and MgB_2, respectively. No diffraction peaks related to sodium-including materials were detected. We also confirmed from X-ray photoelectron spectroscopy (XPS) measurements that

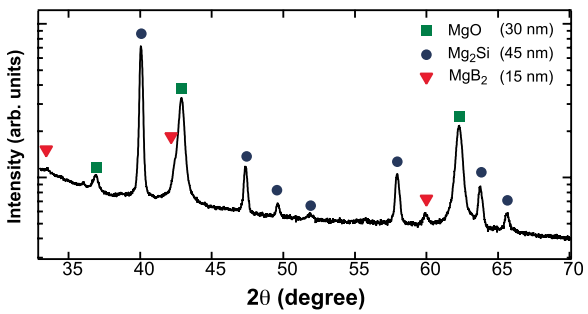

FIG. 1. X-ray diffraction pattern of the reaction zone recorded using Cu Kα radiation (wavelength $\lambda = 1.5418$ Å). Bragg peaks of MgO, Mg_2Si, and MgB_2 phases are indicated. From the full-width at half-maximum of the Bragg peaks and the Scherrer formula, the sizes (lower limit) of MgO, Mg_2Si, and MgB_2 are estimated to be 30, 45, and 15 nm, respectively.

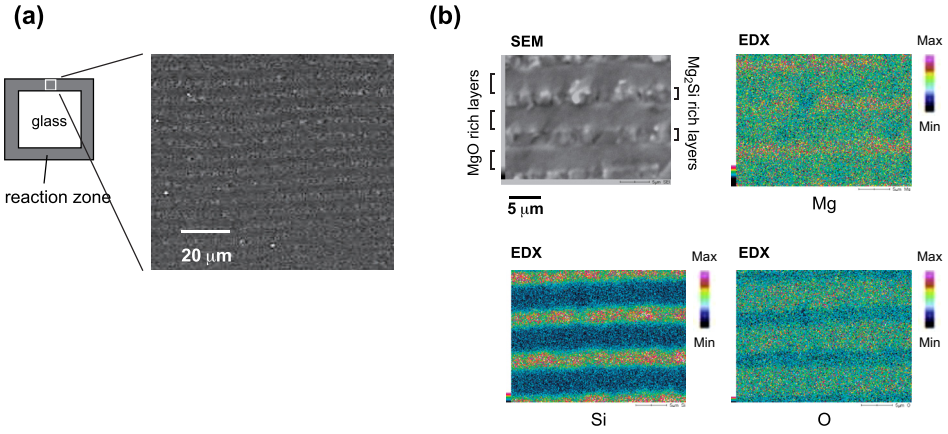

FIG. 2. (a) Schematic representation of the reaction zone created on the surface of the cubic glass sample and a typical low-magnified SEM image of the cross section of the reaction zone. (b) High-magnified SEM image of the reaction zone and the corresponding EDX elemental mapping images of Mg, Si and O. From the EDX analysis, the wider and narrower layers are attributed to the MgO and Mg_2Si-rich layers, respectively.

B and Si are present as boride and silicide anions, respectively, and no signals are detected in the energy region of the Na 1s photoelectrons (Fig. S1[15]). It is hence probable that most Na ions, possibly in the form of Na_2O, are expelled from the reaction zone into the unreacted glassy phase during the reaction. If we assume that the glass with the composition of $68SiO_2$-$24B_2O_3$-$8Na_2O$ (mol. %) reacts fully with Mg via Eqs. (1) and (2), and neglect the contribution from the sodium-related materials, we can estimate the composition of the product as 69 mol. % MgO, 23 mol. % Mg_2Si, and 8 mol. % MgB_2. Assuming the 69MgO-23Mg_2Si-8MgB_2 (mol. %) composition (or 43MgO-49Mg_2Si-8MgB_2 vol. %), we can calculate the ideal density (2.72 g/cm^3) of the product from the molar mass and density of the constituent materials. We found that the sample density measured with a helium pycnometer (2.68–2.73 g/cm^3) agrees well with the ideal density, suggesting that the product is highly dense nanocomposites with no micropores and cracks.

Figure 2(a) shows a scanning electron microscope (SEM) image of the cross section of the reaction zone. As expected from its density, the product does not have any volume defects and pores in the micrometer length scale. One also sees from the SEM image that the reaction zone is characterized by the periodic layered structure with the apparently smooth (wider) and rough (narrower) layers. We found that these periodic layers structures are created all over the reaction zone. Energy dispersive X-ray (EDX) analysis demonstrated that the wider and narrower layers consist mainly of MgO and Mg_2Si, respectively (Fig. 2(b)). Such periodic layer formation has previously been reported to occur during solid-state displacement reaction between Mg and pure silica (SiO_2) glass.[12,16] However, the microscopic layer morphology and detailed growth kinetics of the periodic layer formation have not been fully understood.[12,16–18] For a detailed understanding of the periodic layered structures, we further carried out transmission electron microscopy (TEM) observations. TEM investigations show that the narrower layer consists of relatively large crystallites with a size of a few μm (Fig. 3(a)). Selected area electron diffraction (SAED) measurements of the narrower layer yield a [$\bar{1}$10] zone axis SAED pattern of Mg_2Si (left image in Fig. 3(b)). This indicates that the main component of the narrower layers is Mg_2Si, in consistent with the results of SEM/EDX analysis. On the other hand, the wider layer comprises nanograins with grain sizes of several tens of nanometers (Fig. 3(a)). The corresponding SAED pattern shows ring-like diffraction spots attributed to MgO, Mg_2Si, and MgB_2 nanograins (right image in Fig. 3(b)). Bright-field scanning TEM (BF-STEM) image (Fig. 4(a)) and the EDX elemental mapping (Figs. 4(b)–4(d)) illustrate that the O (blue) and Si-rich (green) regions are mutually exclusive to each other to form maze-like domain structures (see also an overlay mapping of O and Si in Fig. 4(e)). Note also that the B-rich regions (cyan) are present among the MgO and Mg_2Si nanograins (Fig. 4(f)). It should also be worth mentioning that the above

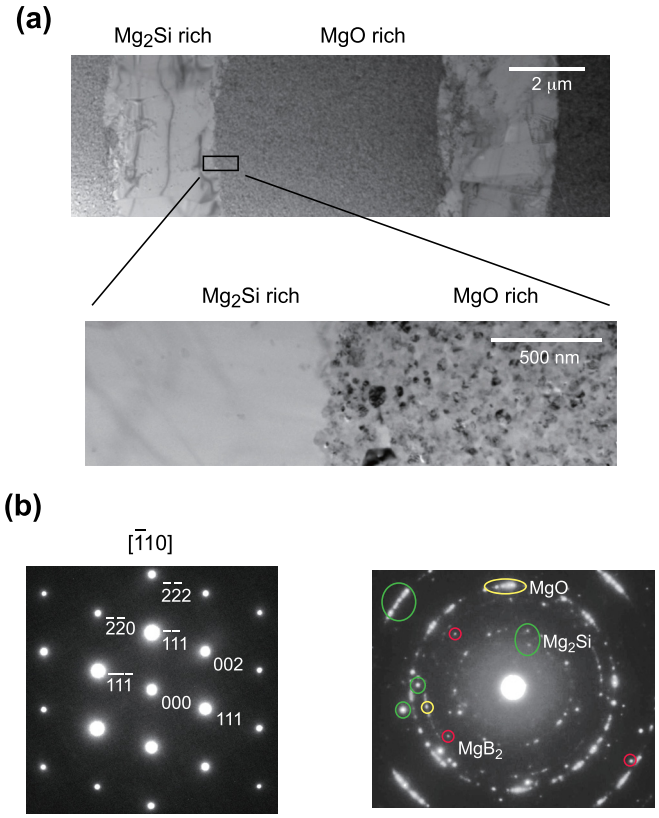

FIG. 3. (a) Low- (top panel) and high-magnified (bottom panel) TEM images of alternating MgO and Mg_2Si-rich layers. (b) SAED patterns of the Mg_2Si-rich layer (left panel) and the MgO-rich layer (right panel). The spotted diffraction pattern of the Mg_2Si-rich layer corresponds to the [$\bar{1}$10] zone axis, whereas the ring-like pattern of the MgO-rich layer indicates the coexistence of MgO (circled in yellow), Mg_2Si (circled in green), and MgB_2 grains (circled in red).

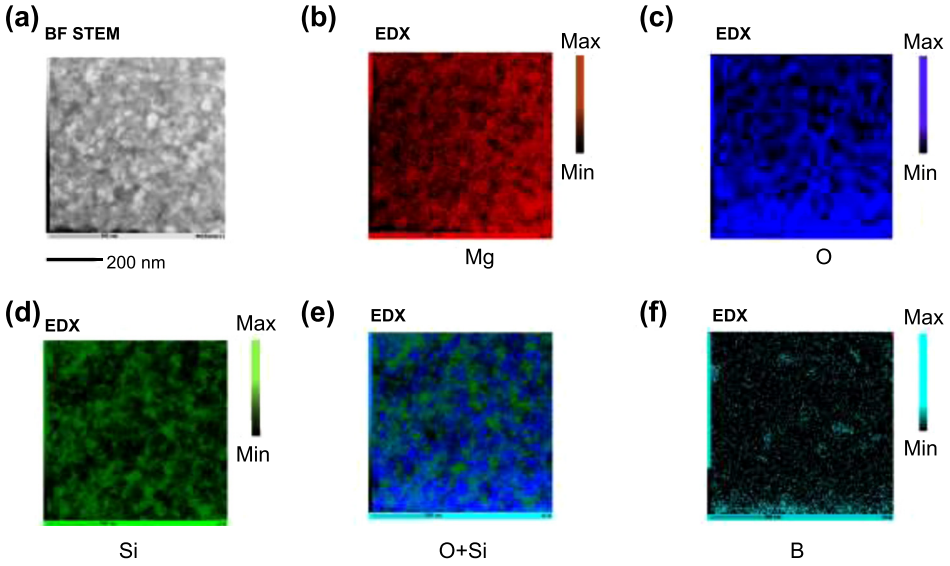

FIG. 4. (a) BF STEM image of the MgO-rich layer and the corresponding EDX elemental mapping images of (b) Mg (red), (c) O (blue), (d) Si (green), (e) overlay mapping of O and Si and (f) B (cyan).

features noted for the narrower and wider layers are similarly observed for all the alternating layers in the sample. From these TEM and EDX analyses and additional high-angle annular dark-field scanning TEM observations (HAADF-STEM) shown in Fig. S2,[15] we can conclude that the wider layers are composed of $MgO/Mg_2Si/MgB_2$ nanocomposites in which MgB_2 nanograins are dispersively embedded in the interconnected MgO and Mg_2Si nanograins. In what follows, however, we will refer to the wider layer as the MgO-rich layer just for the sake of simplicity.

Figure 5(a) shows a typical high-resolution TEM (HRTEM) image of the interface between the MgO and Mg_2Si-rich layers. One sees from Fig. 5(a) that the (111) planes of both MgO and Mg_2Si phases are aligned in the same direction, implying a high lattice coherence at the interface. The lattice relationship between the two crystalline phases can also be investigated by the fast Fourier transform (FFT) analysis of the TEM images (Fig. 5(b)). As expected, the FFT of the Mg_2Si region (see the left image in Fig. 5(b)) yields basically the same pattern as seen in the SAED of the Mg_2Si region of the Mg_2Si-rich layer shown in Fig. 3(b). On the other hand, the FFT of the MgO region of the MgO-rich layer shows two diffraction spots attributed to the (111)-type planes (see the two red arrows in the right image in Fig. 5(b)). The FFT of the interface region (see the middle image in Fig. 5(b)) is the superposition of those of the Mg_2Si and MgO regions and illustrates the alignment of the (111)-type planes of these two crystalline phases; that is, the 111-type spots of MgO are located at the exact center between the 111- and 222-type spots of Mg_2Si.

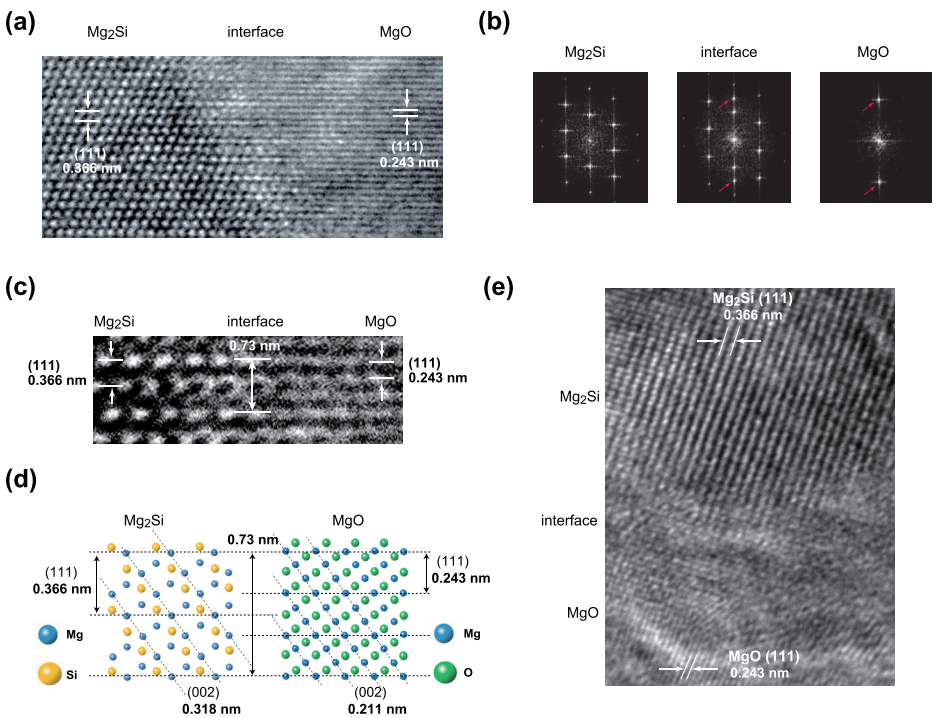

FIG. 5. (a) HR-TEM image of the interface between MgO and Mg_2Si-rich layers. (b) FTT of the HR-TEM images of the Mg_2Si-rich region (left panel), the MgO-rich region (right panel), and the interface region (middle panel). The red arrows correspond to the diffraction spots originated from MgO (111) planes. (c) A magnified view of the HR-TEM image of the interface between MgO and Mg_2Si-rich layers. (d) A 2D schematic illustration of the DME-like structure by atomic models of Mg_2Si and MgO. (e) A typical HR-TEM image of the MgO/Mg_2Si interface in the MgO-rich region.

Detailed inspection of the HRTEM image (Fig. 5(c)) reveals that the interface consists of three MgO (111) and two Mg_2Si (111) planes, resulting in nearly perfectly matched atomic planes with a spacing of 0.73 nm. This derives from the nearly integer ratio of the (111) *d*-spacing of MgO and Mg_2Si crystals (0.243 nm/0.366 nm = 0.664 ≈ 2/3). Considering that MgO and Mg_2Si belong to the same space group of Fm $\bar{3}$ m, we can expect that the 2/3 lattice matching is realized for all the (*hkl*) planes, or all the [*uvw*] directions, at the interface (see the corresponding in-plane atomic structure in Fig. 5(d)).

In thin film growth processes, epitaxial growth is possible as long as the lattice misfit between the film and substrate is less than ∼10%.[19] It has recently been demonstrated, however, that even when a lattice misfit of a given material combination is quite large (more than ∼10%), epitaxial growth could also be possible on the condition that integral multiples of major lattice planes match across the interface.[20] This type of epitaxial growth is called domain matching epitaxial (DME) growth,[20] which is promising for obtaining a coherent or dislocation-free heterostructure in large-lattice mismatch systems.[20–23] Thus, the present 2/3 lattice matching at the Mg_2Si/MgO interface can also be regarded as a type of DME. To our knowledge, this is the first report demonstrating the self-growth of the DME-like interface, since the DME growth generally requires an elaborate and precise control of the deposition conditions such as the deposition rate, the substrate temperature, and the orientation of the substrate.[20–23] A formation mechanism of the periodic layers with the DME-like interface will be discussed in Sec. IV A.

We next investigate the structural and interfacial properties of the MgO-rich regions consisting of MgO, Mg_2Si, and MgB_2 nanograins. Figure 5(e) shows a typical HRTEM image of the interface between Mg_2Si and MgO nanograins in the MgO-rich regions. An ideal DME-like interface as seen in Fig. 5(a) was not observed in Fig. 5(e); however, the interface between the Mg_2Si and MgO nanograins is rather continuous, showing no discrete grain boundaries. This suggests that the atomically smooth MgO/Mg_2Si interfaces are present in the MgO-rich region as well. Unfortunately, the MgB_2-related heterostructures cannot be unambiguously recognized by the present HRTEM measurements because of the low concentration of MgB_2. As will be shown below, however, a clear semiconductor-superconductor transition along with intergrain Josephson coupling transition is observed in the present nanocomposite. This implies that high-quality MgO/Mg_2Si/MgB_2 heterointerfaces are created in the MgO-rich region.

B. Electrical properties

We then move on to the electrical properties of the nanocomposite. To evaluate the resistivity of the periodic layered structure, four-terminal contacts were made on the cross section of the product along the direction parallel to the layers. We then measured the resistivity in the temperature region from 300 down to 4.2 K. As shown in Fig. 6, the room temperature resistivity is ∼5 Ω cm. This value is about two orders of magnitude higher than that of bulk Mg_2Si (∼0.07 Ω cm).[24,25] This increase in resistivity most likely results from the presence of insulating MgO nanograins in the MgO-rich layers. These MgO nanograins are expected to act as tunneling barriers with tunneling resistance.[26] The resistivity of the sample shows the negative temperature coefficient in the 40–300 K region, indicating that the semiconducting Mg_2Si phase in the Mg_2Si- and MgO-rich layers is responsible for the electric transport properties in this temperature region. Upon further cooling, a transition from a semiconducting to a superconducting state is observed at $T = 36$ K, which is slightly lower than the well-recognized superconducting transition temperature (T_c) of the bulk MgB_2 ($T_c = 39$ K).[27] Note also that the slope of the resistivity versus temperature changes at ∼24 K (see the inset of Fig. 6), suggesting the presence of a second transition. In what follows, we refer to the higher and lower transition temperatures as T_{c1} (36 K) and T_{c2} (24 K), respectively. When the temperature of the system drops below ∼17 K, the sample eventually shows near-zero ($\lesssim 10^{-4}$ Ω cm) resistivity.

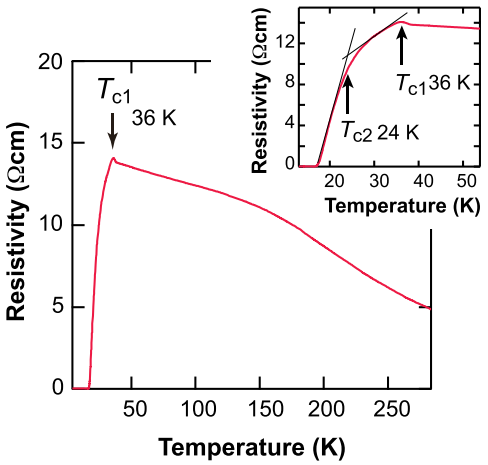

FIG. 6. Electrical resistivity of the cross section of the product as a function of temperature along the direction parallel to the periodic layered structure. The inset shows a magnified view around the transition region, illustrating a two-step transition. The higher and lower-transition temperatures are denoted as T_{c1} and T_{c2}, respectively. T_{c2} is tentatively defined as the point where extrapolations of the linear portions of the resistivity curve intersect.

C. Magnetic properties

To further explore the superconducting properties of the material, we measured the temperature (T) dependence of the magnetic moment (M) of the composite under different external magnetic fields (H). Figure 7 shows one of these observations for zero field cooling (ZFC) and field cooling (FC) processes at $H = 2000$ Oe (for the $M(T)$ curves measured at different fields, see Fig. S3[15]). Both the ZFC and FC curves become diamagnetic from the onset temperature of 36 K, in agreement with T_{c1} obtained by the resistivity measurement. The ZFC and FC curves show the same temperature dependent magnetization in a wide temperature region from 36 to ∼20 K. The point in which ZFC and FC curves separate is defined as the irreversibility temperature (T_{irr}).[28,29] Such a wide reversible temperature range has not been observed previously from bulk MgB_2 but from low-dimensional superconductors, such as cuprate superconductors,[28,30,31] in which

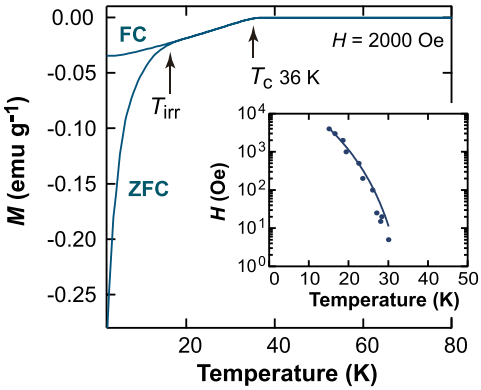

FIG. 7. Temperature dependent magnetization curve under a field of 2000 Oe. FC and ZFC denote the field cooling and zero field cooling, respectively. The inset shows the irreversibility line obtained by performing ZFC and FC measurements under different applied fields from 5 to 5000 Oe. The solid line shows the fitting result using the power low, $H \propto [1-T_{irr}(H)/T_c(0)]^n$. The fitted value of $n = 5.1$ for $T_c(0) = 36$ K.

adjacent superconducting (CuO_2) layers are weakly coupled by the Josephson effect. We found that as shown in the inset of Fig. 7, the field dependence of $T_{irr}(H)$ obeys a simple power law of the type, $H \propto [1-T_{irr}(H)/T_c(0)]^n$ ($n = 5.1$), similar to the case of cuprate superconductors.[28–31] Furthermore, we found that the magnetization $M(H)$ curves have an extremely small or null hysteresis in the temperature region from 36 to ~20 K (Figs. 8(a) and S4[15]), confirming that the present samples are pinning-free superconductors with reversible magnetization characteristics in the temperature region from 36 to ~20 K.

The temperature dependence of the initial $M(H)$ curves is also worth investigating. In the temperature region from 36 to ~25 K, the initial $M(H)$ curve (taken after zero-field cooling) is a straight line under applied magnetic fields at least up to ~2000 Oe (Figs. 8(b) and S5(a)[15]). The initial slope becomes steeper as the temperature of the system decreases (see also the inset of Fig. 8(b)). The point of departure from linearity on the initial $M(H)$ curve represents the lower critical field H_{c1}, which marks the vortex penetration into the superconductor. In the present nanocomposite, the H_{c1} value is estimated to be ~2000 Oe. The observed H_{c1} value is much larger than that of the MgB_2 single crystal (10–30 Oe) in the same temperature region of about 25 to 30 K.[32]

These magnetization properties, i.e., reversible magnetization characteristics, a large increase in H_{c1}, and the temperature (T) dependent $M(H)$ slope, can be reasonably interpreted on the basis of the assumption that the size d of the individual MgB_2 grains is smaller than the penetration depth λ. It has been well documented that when $d < 2\lambda$, its magnetization reduces to $\propto (d/\lambda)^2$ due to appreciable penetration of the applied field, leading to fully reversible $M(H)$ curves.[33,34] Since the crystallite size of MgB_2 in the present nanocomposite is estimated to be 15 nm and the λ values of

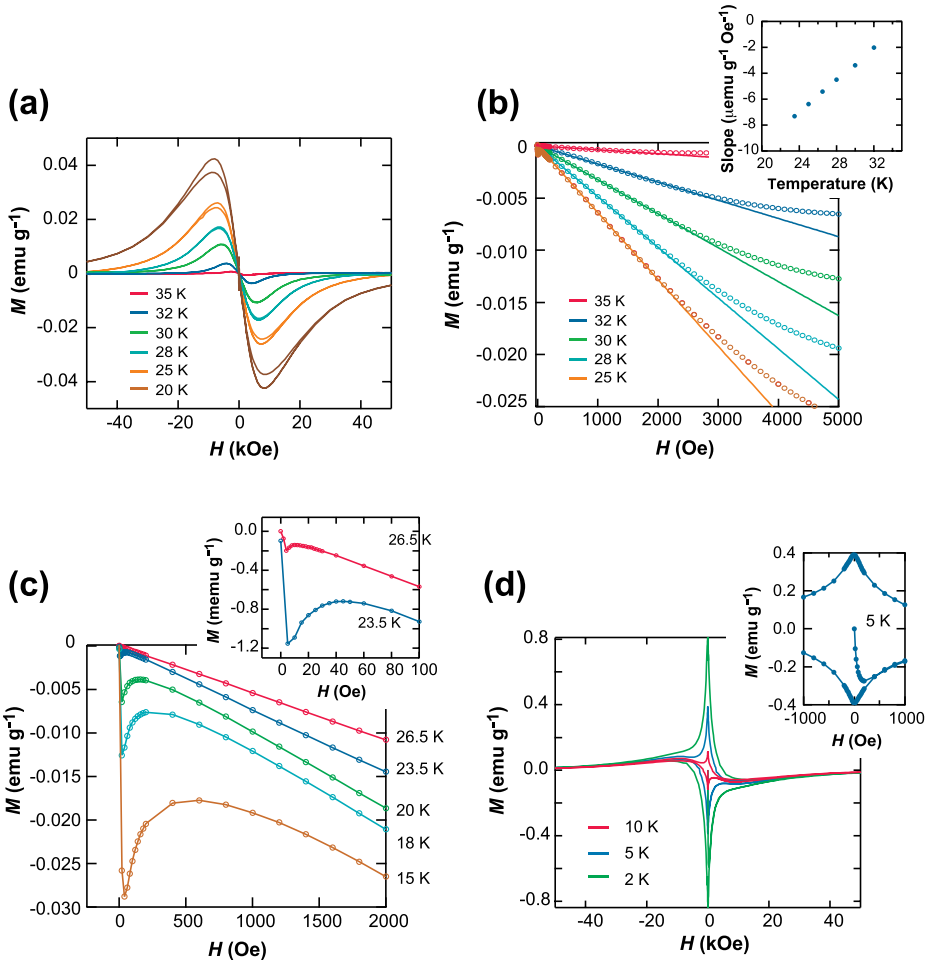

FIG. 8. (a) $M(H)$ curves measured in the temperature region from 20 to 35 K. (b) Initial $M(H)$ curves in the temperature region from 20 to 35 K. The solid lines show the linear fit to the data. The inset shows the temperature dependence of the linear slope. (c) Initial $M(H)$ curves in the temperature region from 15 to 26.5 K. The inset shows a magnified view of the initial $M(H)$ curves at 26.5 and 23.5 K in the near-zero field region. (d) $M(H)$ hysteresis loops measured in the temperature region from 2 to 10 K. The inset shows a magnified view of the $M(H)$ loop at 5 K in the near-zero field region.

bulk MgB_2 are longer than ~100 nm for temperatures above 25 K,[32,35] the condition of $d < 2\lambda$ will certainly be fulfilled in the temperature region from 25 K to T_{c1} (36 K). It should be noted, however, that such ideal reversible magnetization has not been observed from particulate assemblies of compacted MgB_2 nanocrystals with sizes of ~15 nm because of the presence of grain boundaries,[36] which normally exhibit a strong pinning effect.[37] Thus, in the present nanocomposites, atomically clean interfaces with low surface and grain boundary barriers are expected to be present, in agreement with the results of TEM measurements.

Careful investigation of the initial $M(H)$ curves further reveals that an additional diamagnetic component begins to emerge in the low applied field region with decreasing temperature below ~26 K (see Figs. 8(c), S5(b), and S5(c)[15]). The absolute value of the $M(H)$ slope of this newly emerging diamagnetic component, which will be referred to as component A, is at least two orders of magnitude larger than that of the preexisting diamagnetic component, called component B. The deviation from linearity of component A occurs at much lower magnetic fields as compared with that of component B, indicating that the Meissner state related to component A is only stable under very small applied fields. Note also that the width of the $M(H)$ loop increases considerably near the zero field region with decreasing temperature (Figs. 8(d) and S6[15]). These observations demonstrate that the magnetization behavior of component A is highly irreversible in contrast to that of component B. Furthermore, the $M(H)$ loops related to component A show the central peak at $H \approx 0$ Oe (see also the inset in Fig. 8(d) and the insets in Fig. S6[15]).

IV. DISCUSSION

A. Formation model of the periodic layers with domain matching epitaxy (DME) like interface

We have shown from the SEM and TEM measurements that the periodic layered structures are created as a result of the reaction between Mg and a sodium borosilicate glass. The narrower layers consist of micrometer-sized crystallites of Mg_2Si, while the wider layers are composed of nanograins of MgO (main component), Mg_2Si, and MgB_2 (see Figs. 2 and 3). These features are recognized all over the reaction zone, indicating that the basic reaction scheme for the formation of the periodic layers is not changed with reaction time. As noted earlier, such a periodic layered structure has also been reported to be formed in the Mg/SiO_2 system, and several formation mechanisms have been proposed previously.[12,16–18] Thus, we first consider the previous models concerning the formation of alternating MgO- and Mg_2Si-rich layers in the Mg/SiO_2 system.

Although a full consensus has not been reached, it is most likely that the periodic layer formation is derived from the difference in the diffusion rate between Si and Mg in the product.[16] In what follows, we will explain the mechanism on the basis, mainly, of the model proposed by Gutman and his coworkers.[16]

At the reaction front between Mg and SiO_2, the following exothermic reaction initially occurs (Fig. 9(a)):

$$SiO_2 + Mg \rightarrow Si + MgO. \quad (3)$$

The resulting Si reacts further with Mg, leading to the formation of Mg_2Si by

$$Si + 2Mg \rightarrow Mg_2Si. \quad (4)$$

According to the ternary Mg-O-Si diagram, no stable interface exists between Mg_2Si and SiO_2 (Refs. 16–18). Consequently, Mg_2Si will nucleate away from the SiO_2/MgO interface. This leads to the formation of a pair of MgO- and Mg_2Si-rich layers (Fig. 9(b)). The growth rate of the Mg_2Si phase depends on the supply rate of the Si atoms from the reaction front between Mg and SiO_2 to the MgO/Mg_2Si interface. However, the diffusivity of Si atoms in MgO is expected to be quite low.[16] Accordingly, the growth rate of the Mg_2Si phase becomes slow by increasing the thickness of the intervening MgO-rich layer. As a result, some of the Si atoms, along with MgO, newly formed from Eq. (3)

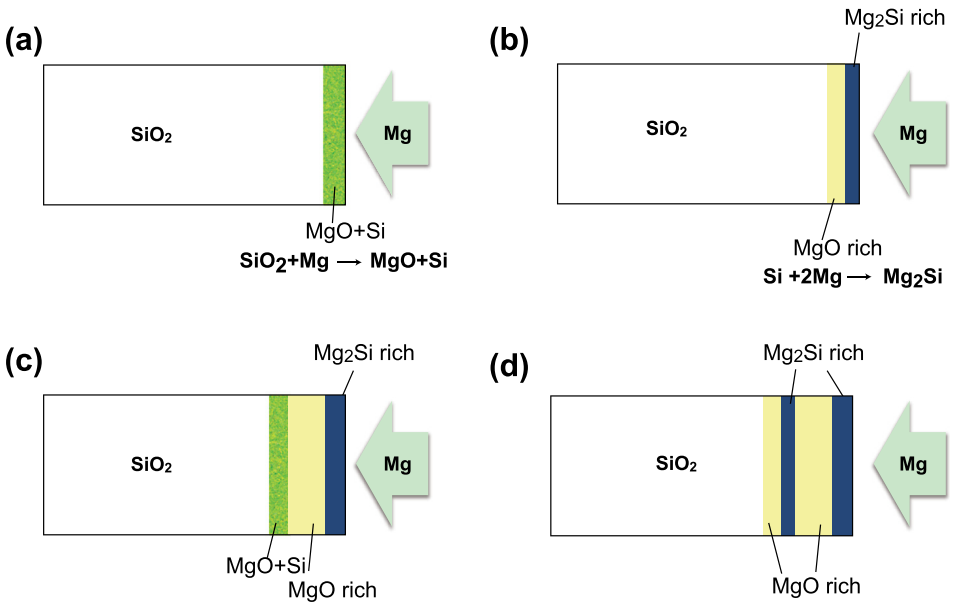

FIG. 9. Schematic representation of periodic structure formation in the Mg/SiO_2 system on the basis of the model proposed by Gutman and his coworkers.[16]

cannot move toward the MgO/Mg_2Si interface but are accumulated near the reaction front (Fig. 9(c)). This indicates that when the thickness of the MgO-rich layer reaches a certain critical value, the existing MgO- and Mg_2Si-rich layer cease to grow. Note, however, that long-range diffusion of Mg atoms through the reaction zone is possible; that is, Mg atoms continue to be supplied from the surface toward the reaction front. When a sufficient amount of Mg atoms is diffused into the reaction front, Mg_2Si can newly nucleate away from the SiO_2/MgO interface (Fig. 9(d)), as in the case of Fig. 9(b), resulting in another set of MgO- and Mg_2Si-rich layers. Further development of alternating MgO-rich and Mg_2Si-rich layers in the Mg/SiO_2 system can thus be expected. The thickness ratio of the thus formed MgO-rich and Mg_2Si-rich layers will be governed by a number of different factors, including the growth rate of the Mg_2Si phase and the diffusion rates of Si and Mg.

As for the present Mg/borosilicate glass system, it is most likely that two-phase periodic layers are formed in a manner similar to the Mg/SiO_2 system. Indeed, preferential nucleation and growth of Mg_2Si are highly expected in the TEM images shown in Fig. 3(a). We should note, however, that the composition of the MgO-rich phase created in the Mg/borosilicate glass system is more complex than that in the Mg/SiO_2 system. That is, in the Mg/borosilicate glass system, the MgO-rich phase consists of MgO, Mg_2Si, and MgB_2. Considering that MgB_2 exists as a liquid phase at temperatures of ~700 °C,[38] we suggest that the MgO-rich phase exists as a liquid-like viscous state during the reaction, which is carried out at 700 °C under Ar atmosphere. On the other hand, Mg_2Si in the Mg_2Si-rich phase will always exist as a solid phase because the melting temperature of pure Mg_2Si is 1102 °C.[39] We hence assume that in the Mg/borosilicate glass system, a liquid-like viscous MgO-rich phase is sandwiched by adjacent solid Mg_2Si-rich phases during the reaction at 700 °C (Fig. 10(a)). Maze-like domain structures observed in the EDX elemental mapping images of the MgO-rich phase (Fig. 4) are consistent with the above assumption because such structures are typically produced by spinodal decomposition of incompressible binary fluid mixtures.[40] The reason for this assumption is that domain matching epitaxy (DME) like structures are observed at the interface between the MgO- and Mg_2Si-rich phases. If the assumption is valid, the formation of the DME like interface can be interpreted in terms of the process similar to liquid phase epitaxy (LPE).[41] The thermodynamic driving force for LPE is generated by cooling the system below the liquidus temperature of the liquid-solid phase diagram.[42] Thus, it can be assumed that the DME like growth of MgO occurs on the Mg_2Si "substrate" during cooling of the system (Fig. 9(b)).

B. Superconducting properties of the $MgO/Mg_2Si/MgB_2$ nanocomposite

We have shown in Sec. III B that the present $MgO/Mg_2Si/MgB_2$ nanocomposite exhibits a two-step resistive superconducting transition characterized by T_{c1} (36 K) and T_{c2} (24 K). Similar two steps of the transition have been found in polycrystalline cuprate superconductors, and the feature is explained on the basis of a granular superconductor.[43] An upper transition temperature defines the temperature in which Cooper pairs appear in the respective grains, whereas a lower one reflects the temperature below which superconducting grains are connected by Josephson effect, resulting in a true zero-resistance superconducting state. This model of a granular superconductor is most likely applied to the present nanocomposite system. That is, T_{c1} (36 K) and T_{c2} (24 K) will correspond to intra- and intergrain superconducting temperatures, respectively, of the MgB_2 nanograins embedded in the MgO-rich layers.

It has previously been recognized that intergrain transition will not happen in granular composites unless the superconducting grains are in intimate physical and electrical contact.[44–46] Indeed, superconducting transition is not normally observed in a granular composite system in which the volume fraction of superconducting grains is below ~50%.[44–46] In the present nanocomposite, however, percolation channels consisting of "physically" connecting MgB_2 nanograins would not be expected to exist. This is because the volume fraction of MgB_2 in the MgO-rich layer is less than ~20 vol. %, which is estimated from the volume composition of the reaction layer (43MgO-49Mg_2Si-8MgB_2 vol. %). Here, we should recall that rather good heterointerfaces are formed in the present nanocomposite. It is hence probable that high-quality Josephson junctions with a low normal state (intergrain) resistance R_N are created in the MgO-rich layers. In addition, the MgO nanograins in the MgO-rich layers will act as tunneling barriers with low tunneling resistance. The present reactions are carried out under Mg-rich and O deficient conditions in Ar atmosphere, and accordingly, a number of oxygen vacancies are expected to be present in the MgO nanograins. These intrinsic defects can provide conduction channels in the MgO-rich layers via

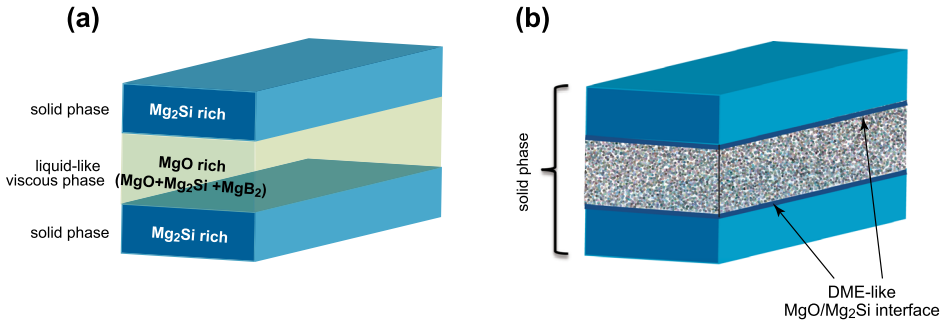

FIG. 10. Schematic representation of the formation of the DME-like interface in the Mg/borosilicate glass system.

electron tunneling,[26,47,48] leading to a decrease in R_N. Consequently, a high Josephson coupling energy E_j is expected since E_j can be expressed via R_N as[49,50]

$$E_j = \frac{\pi\hbar\Delta(T)}{2e^2R_N}\tanh\left(\frac{\Delta(T)}{2k_BT}\right), \quad (5)$$

where $\Delta(T)$ is the temperature dependent energy gap, e is the electron charge, k_B is the Boltzmann's constant, and $\hbar$ is the Planck's constant divided by 2π. When the Josephson-junction coupling energies rise above the thermal energy k_BT and the Coulomb charging energy E_c, the phases of the superconducting wave function on the various grains are locked together to give long-range phase coherence and zero resistance.[43–45] Thus, we suggest that at temperatures below T_{c2}, the condition for the intergrain phase-lock transition, i.e., E_c, $k_BT < E_j$, is satisfied, resulting in the construction of the three-dimensional (3D) Josephson junction network in the MgO-rich layers where the MgB_2 nanograins are embedded. As a result of the strong intergrain coupling, the whole of the MgO-rich layers could be transformed into a superconducting state, and a huge increase in the superconducting volume fraction is expected. This will result not only in the second superconducting transition defined as T_{c2} but also in the strong diamagnetic signals in the low magnetic field region (component A) at temperatures below ~24 K (see Fig. 8(c)).

It has been demonstrated that in a three-dimensional Josephson network, flux quanta penetrate the network irreversibly in much the same way as Abrikosov vortices nucleate in hard type II superconductors.[51] This gives a reasonable account for the large magnetic hysteresis shown in Fig. 8(d). The observed central peak at fields close to 0 Oe is also consistent with this scheme, because such a central peak feature has often been observed in granular superconductors with good intergrain connectivity[52,53] and is attributed to the intergranular supercurrents.[54]

From an applied point of view, it would be useful to evaluate the critical current density as a function of temperature T and applied field H. As for hard type-II superconductors, a magnetic critical density, $J_c(H)$, can be derived from the width of the magnetization loop, $\Delta M(H)$, on the basis of the Bean critical-state model[55] described, for example, by

$$J_c(H) \propto \Delta M(H)/d, \quad (6)$$

for slabs of thickness of $2d$. One necessary condition for using the Bean model is that the magnetization on ascending and descending branches of the hysteresis loop at a given H must corresponds to fully penetrated states. For fully penetrated states, shielding currents circulate in only one sense throughout the volume of the specimen for the upper branch of the hysteresis loop and in the opposite sense for the lower branch. In the present layered sample, however, this condition will not be fulfilled because of the presence of the Mg_2Si-rich layers, which will be in the normal state even at temperatures below T_{c2}. Nonetheless, it is worthwhile to investigate $\Delta M(H)$ because it will represent, although qualitatively, the field dependence of J_c in the superconducting MgO-rich layers of the reaction zone.

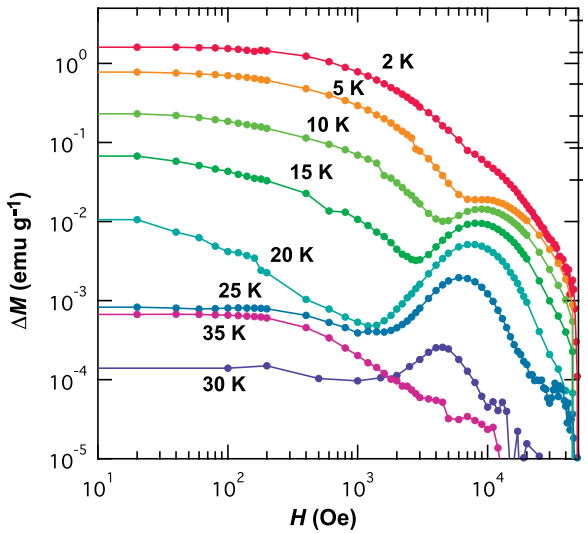

FIG. 11. Width of the hysteresis loops, ΔM, as a function of applied field, H, measured at different temperatures from 35 to 2 K.

Figure 10 shows a field dependence of $\Delta M(H)$ measured at different temperatures from 35 down to 2 K. At a temperature of 35 K, the values of $\Delta M(H)$ are quite small over the entire H region investigated, confirming the weak pinning nature of the respective MgB_2 nanograins just below T_{c1}. As the temperature is decreased to 30 K, one sees a peak in the H region around 5000 Oe. The peak intensity increases and its position shifts to higher fields with further decreasing temperature, as in the case of the peak in the corresponding $M(H)$ loops (see also Fig. 8(a)). That is, the peak features observed in $\Delta M(H)$ and $M(H)$ show a similar temperature and field dependence in terms both of the peak position and the intensity. This indicates that the intragranular magnetization, which will prevail in the temperature region from T_{c1} (36 K) and T_{c2} (24 K), tends to become irreversible with decreasing temperature especially at magnetic fields at which the vortex begins to penetrate into the respective MgB_2 nanograins. Thus, we consider that the peak feature in Fig. 11 is induced by the intragranular screening currents. When the temperature is decreased below ~20 K, a large increase in $\Delta M(H)$ occurs in the low field region below ~1000 Oe. This corresponds to the appearance of component A in the $M(H)$ curves shown in Figs. 8(c) and 8(d). The observed development in $\Delta M(H)$ most likely results from the intergranular screening currents in the assumed three-dimensional Josephson network. It should also be noted that even at a temperature of 2 K, a shoulder peak is observed in the H region around 8000 Oe, hence showing a transition from intergranular to intragranular superconducting screening. Thus, the field and temperature dependence of $\Delta M(H)$ is useful to identify superconducting screening on different length scales.

V. CONCLUSIONS

We demonstrate that fully dense $MgO/Mg_2Si/MgB_2$ nanocomposites consisting of alternating MgO- and Mg_2Si-rich layers are fabricated by solid phase reaction between Mg and a sodium borosilicate glass. Thus, the obtained

nanocomposites are characterized by atomically smooth interfaces. In particular, epitaxial-like growth is observed at the interface between the MgO- and Mg_2Si-rich layers. MgB_2 nanograins are present dispersively in the MgO-rich layers. The resulting $MgO/Mg_2Si/MgB_2$ nanocomposites exhibit a semiconductor-superconductor transition at 36 K, which is followed by a second superconducting transition at ~24 K. The observed two step transition can be interpreted in terms of the intra- and intergrain superconducting transitions. We suggest that the expected high-quality heterointerfaces and the related vacancy-assisted tunneling processes induce "electrically" interacting MgB_2 nanograins to form global superconducting coherence, which can drive the normal state MgO-rich layers into superconducting state irrespective of the small volume fraction of MgB_2. Thus, the present nanocomposites with high-quality interfaces provide a unique granular electronic system, in which MgB_2 nanograins are physically isolated but are electrically interacted to each other, leading to global superconducting coherence via intergrain Josephson coupling.

ACKNOWLEDGMENTS

The support of T. Yamada in the density measurements is acknowledged.

[1]K. Biswas, J. He, I. D. Blum, C.-I. Wu, T. P. Hogan, D. N. Seidman, V. P. Dravid, and G. Kanatzidis, Nature **489**, 414 (2012).
[2]K.-Y. Chun, Y. Oh, J. Rho, J.-H. Ahn, Y.-J. Kim, H. R. Choi, and S. Baik, Nat. Nanotechnol. **5**, 853 (2010).
[3]F. Guo, B. Yang, Y. Yuan, Z. Xiao, Q. Dong, Y. Bi, and J. Huang, Nat. Nanotechnol. **7**, 798 (2012).
[4]J. L. MacManus-Driscoll, P. Zerrer, H. Wang, H. Yang, J. Yoon, A. Fouchet, R. Yu, M. G. Blamire, and Q. Jia, Nat. Mater. **7**, 314 (2008).
[5]J. Gutiérrez, A. Llordés, J. Gázquez, M. Gibert, N. Romà, S. Ricart, A. Pomar, F. Sandiumenge, N. Mestres, T. Puig, and X. Obradors, Nat. Mater. **6**, 367 (2007).
[6]T. C. Shyu, P. F. Damasceno, P. M. Dodd, A. Lamoureux, L. Xu, M. Shlian, M. Shtein, S. C. Glotzer, and N. A. Kotov, Nat. Mater. **14**, 785 (2015).
[7]P. M. Ajayan, L. S. Schadler, and P. V. Braun, *Nanocomposite Science and Technology* (Wiley, Weinheim, 2003).
[8]A. Rosenflanz, M. Frey, B. Endres, T. Anderson, E. Richards, and C. Schardt, Nature **430**, 761 (2004).
[9]R. J. Brook, in *Treatise on Materials Science and Technology*, edited by F. F. Y. Wang (Academic, New York, 1976), Vol. 9, pp. 331–363.
[10]C. P. Cameron and R. Raj, J. Am. Ceram. Soc. **71**, 1031 (1988).
[11]I.-W. Chen and X.-H. Wang, Nature **404**, 168 (2000).
[12]I. Gutman, L. Klinger, I. Gotman, and M. Shapiro, Scr. Mater. **45**, 363 (2001).
[13]T. Uchino, Y. Uenaka, H. Soma, T. Sakurai, and H. Ohta, J. Appl. Phys. **115**, 063910 (2014).
[14]R. J. Charles and F. E. Wagstaff, J. Am. Ceram. Soc. **51**, 16 (1968).
[15]See supplementary material at http://dx.doi.org/10.1063/1.4954875 for XPS spectra, HAADF-STEM images, magnetization as a function of temperature under different applied fields, and detailed $M(H)$ curves.
[16]I. Gutman, I. Gotman, and M. Shapiro, Acta Mater. **54**, 4677 (2006).
[17]Y. C. Chen, J. Xu, X. H. Fan, X. F. Zhang, L. Han, D. Y. Lin, Q. H. Li, and C. Uher, Intermetallics **17**, 920 (2009).
[18]L. Shi, P. Shen, D. Zhang, E. Dong, and Q. Jiang, Appl. Surf. Sci. **274**, 124 (2013).
[19]D. L. Smith, *Thin-Film Deposition* (McGraw-Hill, New York, 1995).
[20]J. Narayan and B. C. Larson, J. Appl. Phys. **93**, 278 (2003).
[21]J. Narayan, Acta Mater. **61**, 2703 (2013).
[22]S. Wang, B. Kavaipatti, S.-J. Kim, X. Pan, R. Ramesh, J. W. Ager III, and L.-W. Wang, Appl. Phys. Lett. **104**, 211605 (2014).
[23]P. Krogstrup, N. L. B. Ziino, W. Chang, S. M. Albrecht, M. H. Madsen, E. Johnson, J. Nygård, C. M. Marcus, and T. S. Jespersen, Nat. Mater. **14**, 400 (2015).
[24]R. G. Morris, R. D. Redin, and G. C. Danielson, Phys. Rev. **109**, 1909 (1958).
[25]G. S. Nolas, D. Wang, and M. Beekman, Phys. Rev. B **76**, 235204 (2007).
[26]F. Schleicher, U. Halisdemir, D. Lacour, M. Gallart, S. Boukari, G. Schmerber, V. Davesne, P. Panissod, D. Halley, H. Majjad, Y. Henry, B. Leconte, A. Boulard, D. Spor, N. Beyer, C. Kieber, E. Sternitzky, O. Cregut, M. Ziegler, F. Montaigne, E. Beaurepaire, P. Gilliot, M. Hehn, and M. Bowen, Nat. Commun. **5**, 4547 (2014).
[27]J. Nagamatsu, N. Nakagawa, T. Muranaka, Y. Zenitani, and J. Akimitsu, Nature **410**, 63 (2001).
[28]K. A. Müller, M. Takashige, and J. G. Bednorz, Phys. Rev. Lett. **58**, 1143 (1987).
[29]J. R. Clem and Z. Hao, Phys. Rev. B **48**, 13774 (1993).
[30]Y. Xu and M. Suenaga, Phys. Rev. B **43**, 5516 (1991).
[31]Y. C. Kim, J. R. Thompson, D. K. Christen, Y. R. Sun, M. Paranthaman, and E. D. Specht, Phys. Rev. B **52**, 4438 (1995).
[32]H.-J. Kim, B. Kang, M.-S. Park, K.-H. Kim, H. S. Lee, and S.-I. Lee, Phys. Rev. B **69**, 184514 (2004).
[33]M. Tinkham, *Introduction to Superconductivity*, 2nd ed. (McGraw-Hill, New York, 1996).
[34]D. M. Gokhfeld, D. A. Balaev, M. I. Petrov, S. I. Popkov, K. A. Shaykhutdinov, and V. V. Val'kov, J. Appl. Phys. **109**, 033904 (2011).
[35]X. H. Chen, Y. Y. Xue, R. L. Meng, and C. W. Chu, Phys. Rev. B **64**, 172501 (2001).
[36]A. Gümbel, J. Eckert, G. Fuchs, K. Nenkov, K.-H. Müller, and L. Schultz, Appl. Phys. Lett. **80**, 2725 (2002).
[37]R. H. Yu, S. Basu, Y. Zhang, A. Parvizi-Majidi, and J. Q. Xiao, J. Appl. Phys. **85**, 6655 (1999).
[38]S. L. Bud'ko, G. Lapertot, C. Petrovic, C. E. Cunningham, N. Anderson, and P. C. Canfield, Phys. Rev. Lett. **86**, 1877 (2001).
[39]G. Busch and U. Winkler, Helv. Phys. Acta **26**, 578 (1953).
[40]T. M. Rogers and R. C. Desai, Phys. Rev. B **39**, 11956 (1989).
[41]H. Nelson, J. Cryst. Growth **27**, 1 (1974).
[42]E. Kuphal, Appl. Phys. A **52**, 380 (1991).
[43]E. A. Early, C. C. Almasan, R. F. Jardim, and M. B. Maple, Phys. Rev. B **47**, 433 (1993).
[44]Y. Shapira and G. Deutscher, Phys. Rev. B **27**, 4463 (1983).
[45]G. Eytan, R. Rosenbaum, D. S. McLachlan, and A. Albers, Phys. Rev. B **48**, 6342 (1993).
[46]A. Gerber, A. Milner, G. Deutscher, M. Karpovsky, and A. Gladkikh, Phys. Rev. Lett. **78**, 4277 (1997).
[47]R. Galceran, Ll. Balcells, C. Martinez-Boubeta, B. Bozzo, J. M. Cisneros-Fernández, M. dela Mata, C. Magén, J. Arbiol, J. Tornos, F. A. Cuellar, Z. Sefrioui, A. Cebollada, F. Golmar, L. E. Hueso, F. Casanova, J. Santamaría, and B. Martinez, Phys. Rev. B **92**, 094428 (2015).
[48]D. J. Kim, W. S. Choi, F. Schleicher, R. H. Shin, S. Boukari, V. Davesne, C. Kieber, J. Arabski, G. Schmerber, E. Beaurepaire, W. Jo, and M. Bowen, Appl. Phys. Lett. **97**, 263502 (2010).
[49]V. Ambegaokar and A. Baratoff, Phys. Rev. Lett. **10**, 486 (1963).
[50]J. D. Hettinger and D. G. Steel, in *High Temperature Superconducting Materials Science and Engineering*, edited by D. Shi (Elsevier, New York, 1995), pp. 21–79.
[51]R. De Luca, S. Pace, C. Auletta, and G. Raiconi, Phys. Rev. B **52**, 7474 (1995).
[52]K.-H. Müller, C. Andrikidis, and Y. C. Guo, Phys. Rev. B **55**, 630 (1997).
[53]W. N. Kang, H.-J. Kim, E.-M. Choi, C. U. Jung, and S.-I. Lee, Science **292**, 1521 (2001).
[54]D. V. Shantsev, M. R. Koblischka, Y. M. Galperin, T. H. Johansen, L. Půst, and M. Jirsa, Phys. Rev. Lett. **82**, 2947 (1999).
[55]C. P. Bean, Rev. Mod. Phys. **36**, 31 (1964).